# Hydrogen trapping and micromechanical behavior in additively manufactured CoCrFeNi high-entropy alloy in as-built and pre-strained conditions

Zhe Gao[1], Dong-Hyun Lee[2], Yakai Zhao[3], Pei Wang[3], Kotaro Murakami[4], Shin-ichi Komazaki[4], Jin-Yoo Suh[5], Hyoung Seop Kim[6], Upadrasta Ramamurty[3,7], Jae-il Jang[1,*]

[1]Division of Materials Science and Engineering, Hanyang University, Seoul 04763, Republic of Korea
[2]Department of Materials Science and Engineering, Chungnam National University, Daejeon 34134, Republic of Korea
[3]Institute of Materials Research and Engineering (IMRE), Agency for Science, Technology and Research (A*STAR), Singapore 138634, Republic of Singapore
[4]Department of Mechanical Engineering, Kagoshima University, Kagoshima 890-0065, Japan
[5]Center for Energy Materials Research, Korea Institute of Science and Technology (KIST), Seoul 02792, Republic of Korea
[6]Graduate Institute of Ferrous & Eco Materials Technology (GIFT), Pohang University of Science and Technology (POSTECH), Pohang 37673, Republic of Korea
[7]School of Mechanical and Aerospace Engineering, Nanyang Technological University, Singapore 639798, Republic of Singapore
*Corresponding author: jijang@hanyang.ac.kr (J.-i. Jang)

## ABSTRACT

The hydrogen trapping and micromechanical behaviors of additively manufactured CoCrFeNi high-entropy alloy (HEA) using the laser powder bed fusion (L-PBF) technique in the as-built and pre-strained states were explored through nanoindentation and micro-tensile experiments combined with thermal desorption analysis. To analyze the influence of pre-straining, both global pre-strains, imposed using the interrupted tensile tests, and local strain levels, estimated using the digital image correlation measurements, were employed. It was revealed that pre-straining (which increases the dislocation density in the alloy) does not enhance the hydrogen effects on the micromechanical performance of the L-PBF HEA. To understand this, rather unexpected, result, we investigated the trapping behavior of diffusional hydrogen in detail, through thermal desorption analysis combined with the Ag decoration technique. The results are discussed in terms of the hydrogen contents and trapping sites in the L-PBF HEA.

**Keywords**: Additive manufacturing, High-entropy alloy, Hydrogen trapping, Nanoindentation.

## 1. Introduction

High-/medium-entropy alloys (H/MEAs) and additive manufacturing (AM) are two topics of research that attracted considerable attention from the structural materials research community in the recent past. The unique microstructural features and mechanical performance of H/MEAs make them candidate materials in various applications [1-5]. The ability to fabricate near-net shaped engineering components with complex geometries, that too in one major processing step, makes metal AM technologies highly interesting from the technological perspective [6-8]. Because of the unique physics of solidification and thermal and thermomechanical fields that the alloy experiences through its melting, solidification, and subsequent layer-wise fabrication, the microstructures (and hence the mechanical performance) of the AM alloys are distinct. Combining these two dimensions of research makes AM of many H/MEAs considerably attractive, and hence is being actively pursued. In particular, alloys processed using the laser-powder bed fusion (L-PBF) technique [9-12] appear to exhibit superior mechanical properties due to (a) the rapid solidification conditions that prevail during L-PBF and (b) several thermo-mechanical cycles that the deposited layers experience subsequently, both of which result in non-equilibrium microstructures including solidification cells whose walls are decorated with segregated solute elements and high densities of dislocations, unconventional crystallographic textures, heterogeneous grain morphologies, and mesoscopic features reminiscent of the melt pools, hatch spacings, and the scanning strategies employed [13-19].

In several industrial application scenarios, structural components can be exposed to hydrogen, which can deteriorate the structural integrity and reliability of it. Consequently, the effect of hydrogen on the mechanical performance of alloys is often studied in detail. The research performed on H/MEAs in this context suggests that H affecting their properties, including embrittling them, is low [20-23]. In particular, the hydrogen-related performance of HEAs with the face-centered cubic (FCC) structures may possibly surpass those of the conventional FCC alloys such as the austenitic stainless steels [24-26]. In consequence, the influence of hydrogen on the mechanical properties of not only conventional HEAs but also AM HEAs have been widely investigated [27-30]. However, detailed studies on the nature of the hydrogen trapping sites in AM HEAs has not yet been performed. This aspect is particularly relevant since several AM alloys, including H/MEAs that are produced used techniques such as L-PBF, have cellular structures with high dislocation densities at the cell boundaries [31-32], which could adversely affect the mechanical performance of H/MEA components that may be deployed in hydrogen environments.

The nanoindentation technique is a powerful tool for examining the effect of hydrogen on the mechanical behavior of alloys (especially, those with the FCC structure) for the following reason. For the hydrogenation of alloys in lab-scale experiments, electrochemical charging is widely used, as it is simple and easy to setup. In electrochemically charged samples, the concentration, $C$, of hydrogen as a function of the distance from the charged surface, $x$, can be estimated using the equation that is derived from the Fick's second law [33-35]:

$$C(x,t_c) = C_0\left[1 - erf\left(\frac{x}{2\sqrt{D_H t_c}}\right)\right] \quad (1)$$

where $C_0$ is the hydrogen concentration at the surface, given by the relation:

$$C_0 = \frac{w \cdot C_M}{4} \sqrt{\frac{\pi}{D_H t_c}} \tag{2}$$

in which $D_H$ is the hydrogen diffusivity, $t_c$ is the charging time, $w$ is sample thickness, and $C_M$ is the mean H concentration in the sample. It is well known that the FCC metals and alloys tend to have a higher hydrogen solubility, but a much lower $D_H$, than the body-centered cubic (BCC) materials [36-38]. As a result, the concentration profile of the charged hydrogen tends to be steep. A representative example of the estimated hydrogen content variation is provided in Fig. S1 of the Supplementary Material. As seen from it, most of the charged hydrogen is confined to a very shallow depth from the charged surface. Since this thickness is only a small fraction of the overall thickness of the tensile specimen, the influence of hydrogen on the tensile response, if any, is likely to be dominated by the remaining pristine alloy's response. However, the responses from nanoindentation tests (in general, with the maximum displacement much less than a few μm) can successfully show the hydrogen-induced changes to the mechanical performance of the alloy.

Keeping the above in view, here we systematically explore the hydrogen trapping and micromechanical behavior of L-PBF CoCrFeNi HEA in two different states (i.e., as-built, and pre-strained) through a series of thermal desorption spectroscopy (TDS) experiments and nanoindentation tests. The CoCrFeNi HEA chosen for examination is known to exhibit superior resistance to hydrogen embrittlement (HE) compared to the more extensively studied CoCrFeMnNi alloy, which is partly attributed to Mn's role in promoting hydrogen-related intergranular fracture [39-41].

The specific objectives of the present study are the following two: (1) Examine whether pre-straining can enlarge the hydrogen effects on mechanical behavior of the AM HEA. Since the pre-straining can significantly increase the dislocation density within the alloy [42-44], which, in turn, enhance the hydrogen trapping within it [45-49], it is reasonable to expect that pre-straining can alter the effects of hydrogen on the mechanical response of the alloy in a significant manner. Thus, a detailed investigation on the interplay between the level of pre-straining and hydrogen effects is essential for understanding the role of microstructures play, in terms of the hydrogen effect on their mechanical performance. (2) Investigate the hydrogen trapping sites in AM HEA. As mentioned above, the detailed analysis of the tapping sites is crucial to capture the role of each crystalline defect in the hydrogen effects, but has not been performed yet.

## 2. Experimental

The CoCrFeNi HEA blocks with the dimensions of 35 × 14 × 38 $mm^3$ were fabricated using a commercial L-PBF machine (TRUMPF, Germany) with the layer thickness, laser power, hatch spacing, and scan speed of 30 μm, 175 W, 100 μm, and 240 mm/s, respectively. This parameter combination was arrived at after an extensive prior-process parameter optimization study. For comparison purpose, a conventionally manufactured (CM) CoCrFeNi HEA sample was prepared by vacuum induction melting followed by hot rolling, homogenization (at 1000°C for 1 h), and water-quenching [50]. Microstructural characterization was conducted using X-ray diffraction (XRD; D8 Advance, Bruker AXS, Germany) and scanning electron microscopy (SEM; Merlin Compact, Carl Zeiss, Germany) with capabilities of electron

channeling contrast imaging (ECCI) and electron backscattered diffraction (EBSD; Hikari, EDAX, USA). Fig. 1 shows a representative inverse pole figure (IPF) map from EBSD analysis that was conducted on the side surface (parallel to the build direction, BD) of as-built L-PBF sample. The average size of the observed columnar grains is ~82 μm and the fraction of low-angle grain boundaries (LAGBs) is ~68.2% of the total grain boundaries (GBs). More detailed information about typical microstructure and deformation behavior of L-PBF processed CoCrFeNi HEA can be found in references [51-55].

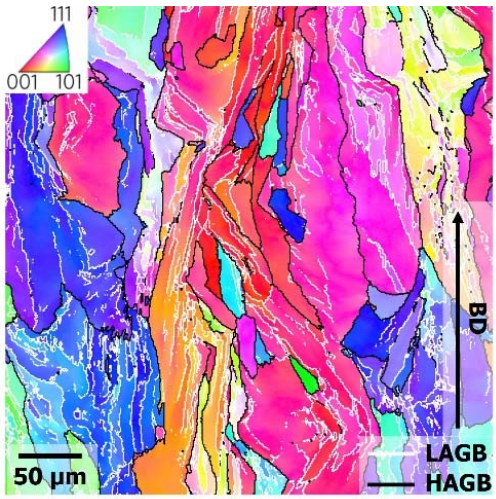


Fig. 1. EBSD IPF map of the as-built sample (LAGB and HAGB: large- and high-angle grain boundaries, respectively).

Uniaxial tensile tests on dog-bone-shaped plate specimens with gauge length, width and thickness of 10, 1, 1 mm respectively were carried out at room temperature (RT) using a micro-tensile tester (MINOS-001, MTDI, Korea) under a strain rate of ~$10^{-4}$ $s^{-1}$. The test was interrupted when the engineering strain (estimated using the crosshead displacement) reached a predetermined value (5, 10, and 15%). The digital image correlation (DIC) technique was

employed to estimate the local plastic strain during tensile deformation and the obtained data were analyzed using the Aramis software (GOM, Germany). At least three tests were conducted for each condition to confirm the reproducibility of the results.

For nanoindentation, sample surfaces were mechanically polished with sandpaper (grit number up to 2000) and then electro-polished at 60 V for 35 s at RT in a mixture of 90% acetic and 10% perchloric acid. Nanoindentation experiments were performed using the Nanoindenter-XP equipment (KLA, USA) with two different three-sided pyramidal indenter tips (i.e., Berkovich and cube-corner) under a constant indentation strain rate of 0.05 $s^{-1}$. After nanoindentation, hardness impressions were profiled using atomic force microscopy (AFM; XE-100, Park Systems, Korea).

Hydrogen was electrochemically charged at RT with potentiostat/galvanostat equipment (HA151A, Hokuto Denko, Japan) in an electrolytic solution of NaOH (0.1 mol/L) and $NH_4SCN$ (0.5 wt.%) for 24 h, and the same current density of 100 mA/$cm^2$ was adopted for all the samples. For quantifying the hydrogen absorbed, thermal desorption spectroscopy (TDS) analysis using a gas chromatographer (JTF-20A, J-Science Lab, Japan) was performed at four different heating rates of 50, 100, 150, and 200 °C/h. The sizes of all the specimens using for TDS (rectangular in shape) were fixed as 5 × 1 × 1 $mm^3$. In addition, for observing the hydrogen distribution, Ag decoration was performed. The hydrogen-charged surfaces were gently polished with 0.02 μm silica suspension, subsequently rinsed with water, and then immersed into an aqueous 4.3 mmol/L $Ag[K(CN)_2]$ solution for 5 min. Then, the decorated surfaces were analyzed via ECCI.

### 3. Influence of pre-straining: global vs. local strain

Since the strain imposed is not always uniformly distributed with the tensile specimens, the level of pre-strain induced is monitored in two different ways. In the first, the 'global' pre-strain imposed was estimated using the interrupted tensile tests. In the second, DIC measurements were utilized to characterize the local strain. Fig. 2 displays the true stress vs. true strain response (measured until failure of the specimen) superimposed with the responses from the interrupted tensile tests for pre-strains of 5, 10, and 15%. In all the tensile tests, the loading axis was normal to BD of L-PBF, as shown in Fig. S2 of Supplementary Material. Note that the specimens taken normal to BD were reported to show higher strength and ductility than those along BD, possibly because the fraction of melt pool boundaries normal to BD is lower [56-57]. The inherent microstructural heterogeneity in a tensile specimen results in a non-uniform strain distribution even in the early stages of deformation, as shown in Fig. 2. It is likely to be more pronounced in the AM alloys (due to their meso-structural nature) and clearer in micro-sized sample (due to the magnified microstructure and thus strain distribution). Such inhomogeneous strain distributions in the DIC results of AM samples were also reported in literature [58-60].

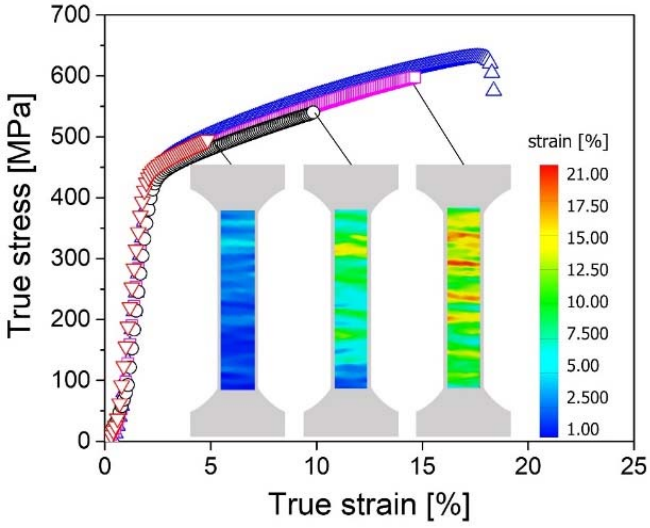


Fig. 2. Representative true stress-true strain curves obtained from the tensile tests. Insets show local strain distribution measured using the DIC technique.

The variation in dislocation density ($\rho$) in the as-built and pre-strained samples were estimated using the XRD analysis for which the "whole" gauge part of a tensile specimen was used. The modified Williamson-Hall method, aided by the modified Warren-Averbach method, was employed to estimate $\rho$ from the full width at half maximum (FWHM) values of the diffraction peaks in the XRD results, details of which are provided elsewhere [61-63]. The results are shown in Fig. 3. The estimated $\rho$ value in the as-built L-PBF sample (~$2.28 \times 10^{14}$ $m^{-2}$) is found to similar to that reported for CoCrFeMnNi HEA [64]. As expected, $\rho$ increases with the pre-strain.

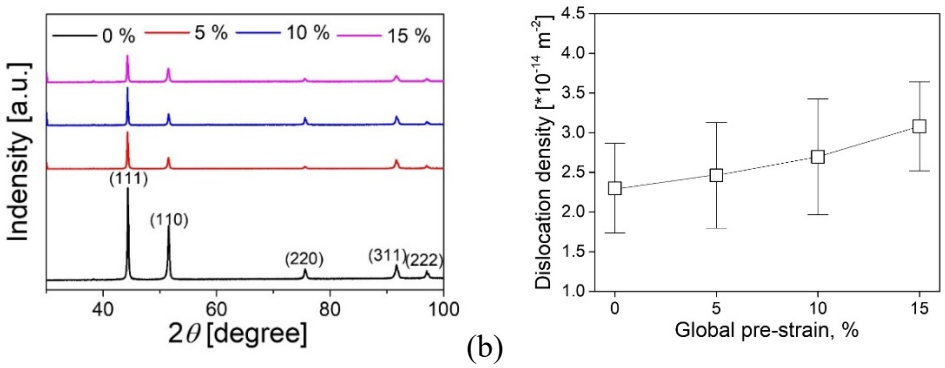


Fig. 3. (a) X-ray diffraction scan results and (b) variation in dislocation density with global pre-strain. The average values with standard deviations in (b) are from the five peaks for different planes in (a).

From the DIC results displayed in Fig. 2, it is seen that the strain distribution within the specimens that were subjected to larger pre-strains is highly nonuniform. For example, the local strains values in the sample subjected to a 15% pre-strain sample vary from 8 to 21%, due to the geometry of the small-sized thin specimens. Another way to explore the pre-straining effect is to use such local strain variation in the DIC images. Although such variations may be deemed as 'undesirable' in the context of a uniaxial test, they can be exploited in the current context since different levels of pre-strain can be achieved within a single tensile-test specimen. To examine the appropriateness in using local pre-strains measured by DIC, the nanoindentation results from three regions for different "local" pre-strain (8, 12, and 21%) in the 15% (global) pre-strained sample were compared in Fig. 4 with those from the central regions of the gauge parts of the three specimens pre-strained to different "global" levels (5, 10, and 15%). Similar hardness values for similar pre-strains were indeed achieved, confirming the DIC-based approach is valid and thus can be an efficient way for analyzing the pre-straining effect. Thus, following nanoindentation tests and the related analyses for exploring the hydrogenation effect

were performed at the regions having different "local" pre-strains within the 15% pre-strained specimen.

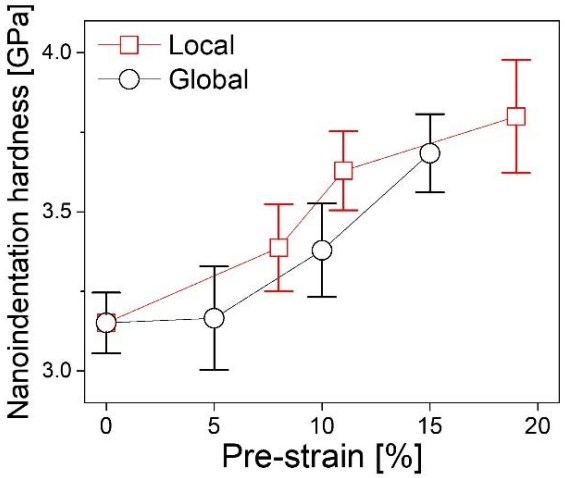


Fig. 4. Variations in nanoindentation hardness with increasing strain. The average values and standard deviations are from 15 tests performed with identical testing conditions.

Another feature in Fig. 4 is a consistent increase in nanoindentation hardness with increasing pre-strain level, regardless of the pre-strain type (either global or local). This strain hardening behavior can be well explained by the increase in $\rho$ (Fig. 3). Microstructural evolution in the three different regions of "local" pre-strains was analyzed with the aid of ECCI, as shown in Fig. 5. In the undeformed state, the microstructure of the as-built sample (Fig. 5a) exhibits a solidification cell structure where the cell walls contain high-density dislocations [30, 65]. With a pre-strain of 8% (Fig. 5b), the cell structure becomes less pronounced and some slip lines (marked by arrows) are observed. At 14% (Fig. 5c), development of mechanical twins with a thickness of a few nanometers are seen, and eventually, at 21% (Fig. 5d), significant amounts of primary and secondary twins were evident. Note that the mechanical twins are often

identified as linear bands with sharp contrast (as indicated by the arrows in Figs. 5c and 5d) [30, 66].

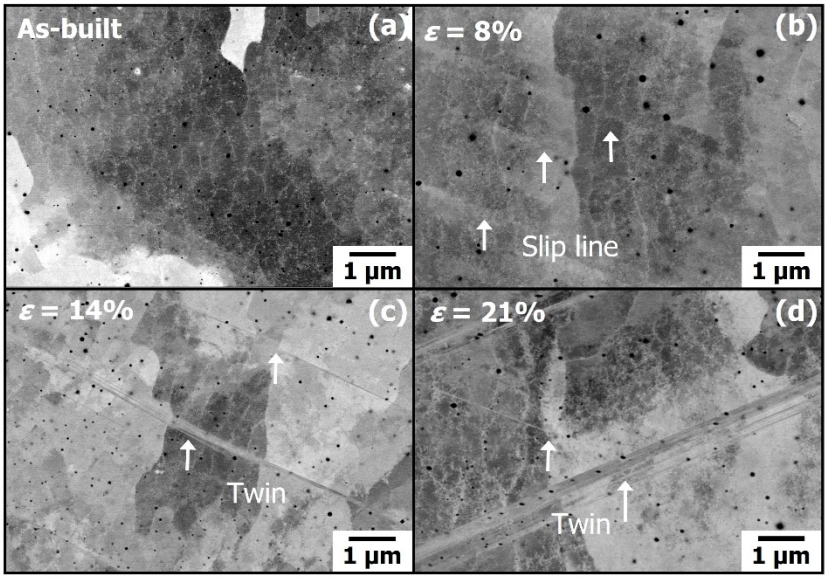


Fig. 5. TEM micrographs showing the microstructural evolution with local pre-straining.

## 4. Hydrogen effect in the as-built and pre-strained samples

Variations in the nanoindentation results with different local pre-strains are plotted in Fig. 6 for both hydrogen-charged and uncharged conditions. The hardness values in both the conditions increase continuously with the pre-strain. The most interesting feature in the figure is that the hydrogenation-induced hardness change is almost negligible for all the conditions, which is different from the general expectation that a material having a larger amount of crystalline defects may exhibit more pronounced variations in its mechanical behavior due to the charged hydrogen In Fig. 6, the variations in $h_f/h_{max}$, where $h_f$ is the final indentation displacement after unloading and $h_{max}$ is the maximum displacement, are plotted against the

local pre-strain level. The $h_f/h_{max}$ ratio is often referred to as 'indentation plasticity index' and is well-known as a good indicator for the deformability of the indented material [63]. Although the values of $h_f/h_{max}$ for all examined samples are reduced after hydrogen charging, it is evident the reduction is neither significant (< 0.05) nor dependent on pre-strain. Thus, the nanoindentation results in presented in Fig. 6 suggest that pre-straining does not amplify the hydrogen effects on the mechanical behavior in the examined AM HEA.

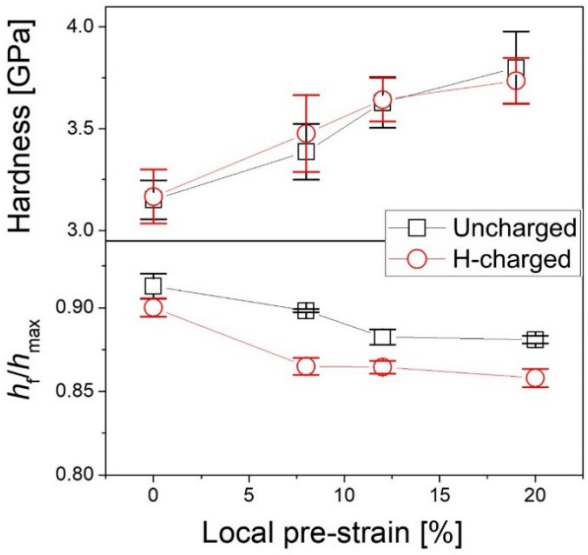


Fig. 6. Variations in nanoindentation hardness and $h_f/h_{max}$ with local pre-strain under uncharged and hydrogen-charged states.

During indentation, some portion of the material deformed from within the indented volume can 'pile-up' around the indentation impression. Fig. 7 shows the topography resulting from indentations of as-built and largely pre-strained (for local strain of 21%) samples and the change in pile-up ratio, $h_{pile\text{-}up}/h_r$, where $h_{pile\text{-}up}$ and $h_r$ (both measured using AFM) are the pile-up height and remaining displacement after unloading, respectively. All indentations for Fig. 7

were made with a cube-corner indenter that is sharper and thus can produce more pronounced pile-up than the commonly used Berkovich indenter [67-68].

Pile-up is expected to become larger for a material having a smaller strain hardening exponent, i.e., a material having a lower ability to accommodate the indentation-induced plastic deformation through work hardening [69-70]. Large pre-straining can cause a significant increase in dislocation density and thus can make additional strain hardening difficult. Thus, the pile-up behavior in the regions with larger pre-strain is expected to be more pronounced than that in the as-built sample. In Fig. 7, the pile-up ratio, $h_{\text{pile-up}}/h_{\text{r}}$, is used (instead of just $h_{\text{pile-up}}$) because the pile-up amount (or $h_{\text{pile-up}}$) is dependent not only on such hardening ability but also on the volume removed during indentation (or $h_{\text{r}}$). Thus a simple comparison of the $h_{\text{pile-up}}$ between the materials having different $h_{\text{r}}$ may not be correct. In Fig. 7, it is interesting that, although the pile-up ratio is significantly enhanced by pre-straining, hydrogen charging does not seriously alter the ratio in both samples (only marginal decrease in hydrogen-charged as-built sample). Along with the hardness change (in Fig. 6), this observation further supports the conclusion that pre-straining does not alter the hydrogen effects on the mechanical behavior of this AM HEA.

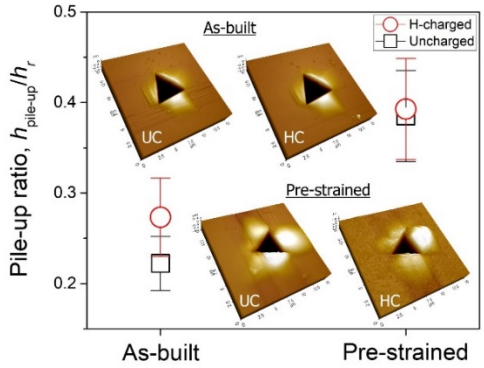

Fig. 7. Variations in pile-up ratio with representative indentation surface profiles obtained from AFM.

## 5. Hydrogen trapping behavior and its effects

The most important question arising from the above results is why pre-straining does not alter the hydrogen effect despite a substantial increase in the dislocation density in the alloy due to pre-straining. For addressing this, a comprehensive understating of the hydrogen trapping behavior in both as-built and pre-strained samples is required.

Although the observation of H atoms within the trap sites would provide a direct evidence, it was not experimentally possible as of now. While the detection of hydrogen through TEM is only possible in highly specific cases, such as hydrogen on graphene [71], it is almost impossible in alloys. Recently, Chen *et al*. [72] reported that individual hydrogen atoms at trapping sites in a ferritic steel were directly observed via atom probe tomography (APT) analysis. However, as pointed out in that study, the origin of hydrogen detected is ambiguous (primarily by a contaminant from a high vacuum chamber), and thus deuterium (D or $^{2}$H) was used instead of hydrogen. Also, APT's limitation in analyzing only small volume of material makes it less suitable for providing a definitive proof for the conclusions we reached. Therefore, in the present study, TDS analysis with Ag decoration was adopted to experimentally confirm the trapping behavior in a comprehensive way.

First, we employed the Ag decoration technique with which one can qualitatively analyze the distribution of "diffusible" hydrogen (weakly bonded with microstructure and thus plays the main role in hydrogen-induced mechanical performance variations) [73-74]. In this

simple chemical method, the hydrogen atoms adsorbed on the surface transform Ag ions into elemental Ag through the reaction, $Ag^+ + H \rightarrow Ag + H^+$, and thus the sites where white Ag particles are observed can be considered as the hydrogen enriched ones. Fig. 8 presents the representative SEM images of the hydrogen-charged samples after immersion in the Ag decoration solution. In the surface images of both the as-built and pre-strained samples, the Ag particles are randomly distributed and there is no specific shape or trend that could correspond to any type of crystalline defects; i.e., there is no obvious trend for hydrogen atoms (manifest as white Ag particles in the images) to be enriched in either the solidification cell walls in as-built sample (Figs. 8a and 8b) or the deformation twins in the pre-strained sample (Figs. 8c and 8d), which have been often identified as hydrogen trapping sites [75-76]. This observation suggests that diffusible hydrogen mainly resides at the interstitial lattice sites (and perhaps some dislocations inside the cells) rather than at solidification cell walls or mechanical twins. It is noteworthy that the dislocation-tangled cell walls in a L-PBF specimen is known to be energetically stable (due to the pinning effects by the segregated elements and/or oxides) [77-78]. Because of the relatively stable state of the cell walls, it is conceivable that the walls' potential energy landscape for hydrogen is shallower than that of other defects. This makes the dislocation-tangled walls unfavorable residing sites for hydrogen, which is a distinct feature from that of the typical dislocations observed in conventional alloys [77-78]. In addition, one can also imagine that the lattice in HEA may play a more active role in trapping of diffusible hydrogen than that in conventional alloys (that have only one or two principal elements) due to the well-known lattice distortion in HEAs [24,26,41].

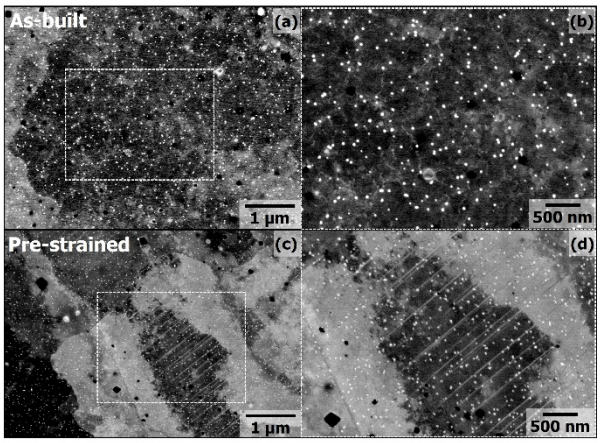


Fig. 8. Representative ECCI images of the as-built (a,b) and pre-strained (for a local strain of 18%) samples (c,d) after immersion in Ag decoration solution.

To conduct more detailed analysis of the hydrogen trapping behavior in a quantitative manner, TDS was performed on as-built samples under four heating rates (50, 100, 150, and 200 °C/h). As shown in Fig. 9a, all the TDS curves exhibit two distinct peaks. It is often accepted that the low- and high-temperature peaks correspond to the desorption of diffusible and non-diffusible hydrogen, respectively [63, 79-82]. The estimated hydrogen contents from the four curves were similar, and in the range of 14~19 wppm. In addition to the hydrogen quantities, analysis of the curves obtained under various heating rates can provide a clue for identifying the possible sites for hydrogen trapping. From TDS data, the apparent activation energy for hydrogen desorption from each trapping site can be calculated by using the Kissinger's equation:

$$\frac{\partial \ln\left(\frac{\emptyset}{T_P^2}\right)}{\partial \frac{1}{T_P}} = -\frac{E_a}{R} \tag{3}$$

where $\Phi$ is the heating rate, $T_p$ is the temperature at which the maximum in the desorption peak occurs, $E_a$ is the activation energy for hydrogen desorption, and $R$ is the universal gas constant

[83-84]. The results of the fits to the TDS data plotted on a log-log scale (following the left-hand term of Eq. (3)) are shown in Fig. 9b. The apparent activation energies for low- and high-temperature peaks (corresponding to diffusible and non-diffusible hydrogen desorption) were estimated to be ~36 and ~60 kJ/mol, respectively. The results are in a good agreement with the fact that the activation energy for diffusible hydrogen (weakly bonded with microstructure) is lower than that for non-diffusible hydrogen (characterized by a strong binding affinity) [85-89].

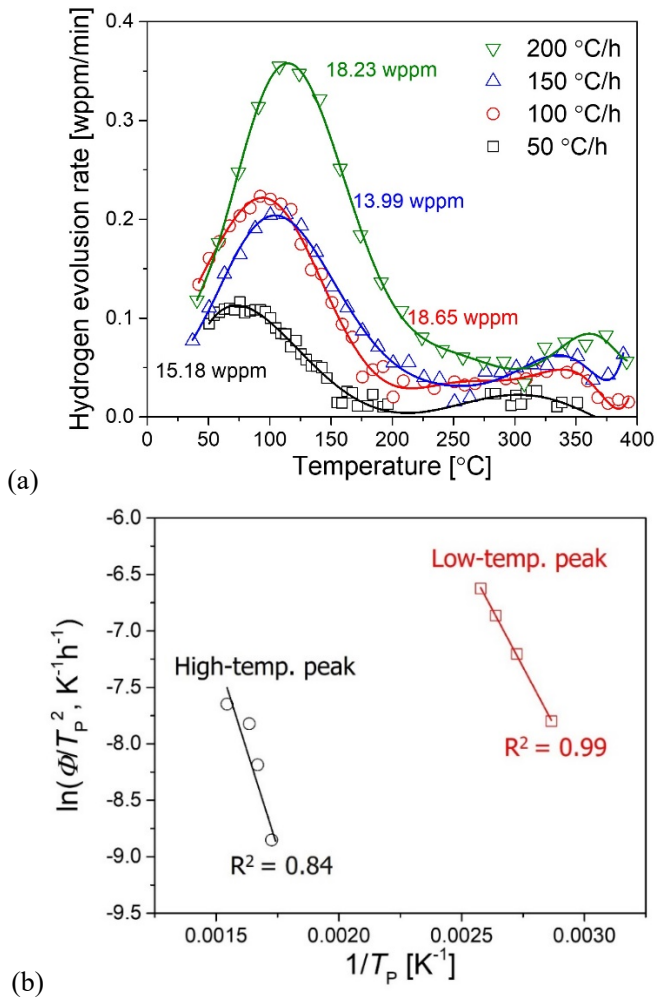


Fig. 9. (a) TDS curves of as-built samples obtained under different heating rates and (b) Kissinger plots and activation energies for the low- and high-temperature peaks.

Strongly trapped non-diffusible hydrogen is immobile at RT and hence is not expected to deteriorate the mechanical performance in a significant manner [90-93]. In Fig. 9b, the activation energy value for non-diffusible hydrogen (~60 kJ/mol) closely aligns with the reported value for micro-voids (~56 kJ/mol) [94], thereby suggesting a possibility that the trapping sites for non-diffusible hydrogen in the present study may be the porosity that is inevitable in the AM processed alloys. This scenario can be supported by comparing the TDS curve of AM sample with that of CM counterpart sample (Fig.10). While similar low-temperature peaks were observed in both the samples, high-temperature peak was only detected in the AM sample. The absence of the high-temperature peak in the CM sample suggests that the hydrogen trapping sites associated with it may be the porosity produced during AM process. Another important feature to be noted from Fig. 10 is that the low-temperature peak for AM sample completely overlaps with that for CM sample. This observation provides additional evidence that the solidification cell walls in the AM sample have almost a negligible effect on the hydrogen trapping behavior in the present alloy.

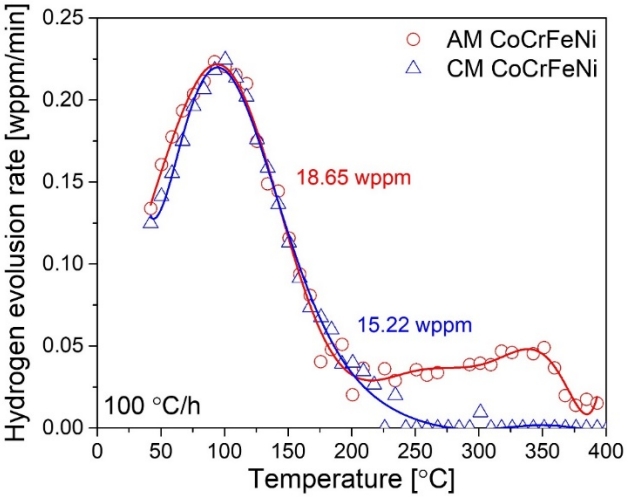

Fig. 10. Comparison of TDS results obtained from the AM and CM CoCrFeNi samples. Lines are drawn through the data for the purpose of guiding the eye.

Unlike non-diffusible hydrogen, diffusible hydrogen is mainly responsible for the hydrogen effect on mechanical properties because it can relatively easily diffuse in a material at RT due to the low activation barrier. The low-temperature peak for diffusible hydrogen can be the merged result from many different microstructural features. In this sense, we employed a deconvolution methodology to yield more lucid and comprehensive insight into the trapping sites of diffusible hydrogen. The highest number of the appropriately deconvoluted peaks in this study was three, as illustrated in Fig. 11; i.e., despite repeated attempts, the decomposition into four peaks was not successful.

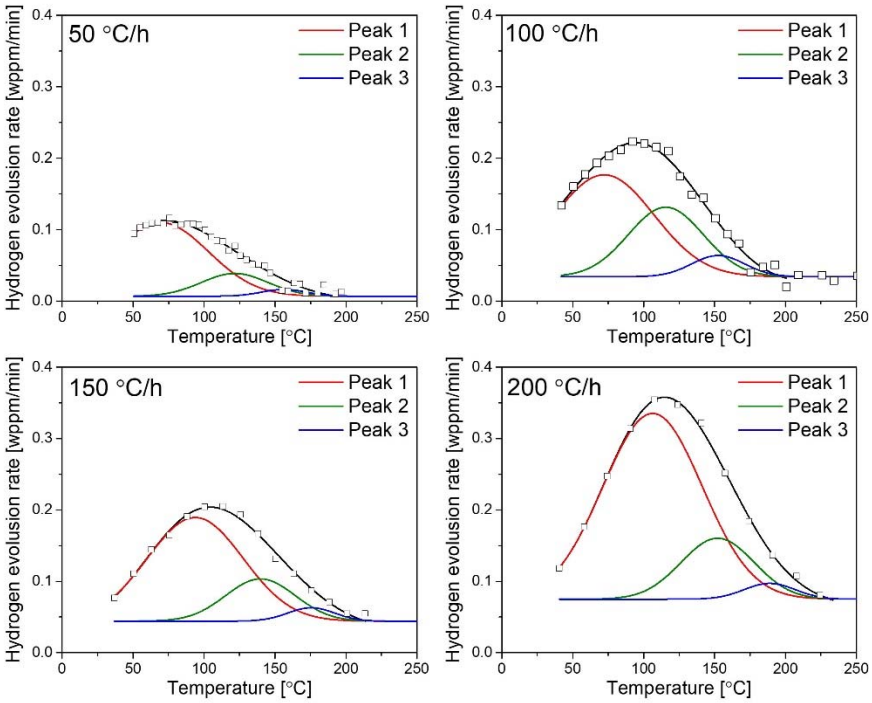


Fig. 11. Results from the decomposition of the low-temperature peaks for as-built sample.

From three deconvoluted peaks for 4 different heating rates, the activation energy for diffusible hydrogen desorption from each peak was estimated. Fig. 12 shows the plots following Eq. (3) and the apparent activation energy values for the peaks were determined as 23.6, 45.3, and 62.3 kJ/mol for Peak 1, 2, and 3 in Fig. 11, respectively. For comparison purpose, with the estimated energies in this study, Fig. 13 summarizes the values of activation energy for diffusible hydrogen desorption for FCC metallic materials and body-centered cubic (BCC) Fe, reported in the previous studies where multiple trapping sites were examined [83-84, 95-99]. (More detailed information about Fig. 13 is provided in Table S1 of Supplementary Material.) The literature values of the activation energies for the trapping sites for diffusible hydrogen demonstrates a clear trend, where the value increases in the order of lattice, dislocation, and vacancy sites. In consideration of the activation energy values and the changing trend with the defects, it is reasonable to suggest that Peaks 1, 2, and 3 in Fig. 12 correspond to lattice, dislocation, and vacancy, respectively. It should be noted that, normally the activation energies for dislocations and grain boundaries are very close to each other and hence are difficult to distinguish [83, 100-101]. In the present study, however, the results from Ag decoration (Fig. 8) demonstrates very few Ag particles along the grain boundaries whereas the vast majority of the particles are inside the grains. This indicates that hydrogen atoms are mostly enriched in lattice and/or dislocations and much less in grain boundaries. Therefore, here we consider Peak 2 as corresponding to that of the hydrogen predominantly desorbing from dislocations. Since the area under each peak in Fig. 11 is directly proportional to the

diffusible hydrogen amount, the largest amount of hydrogen is believed to be weakly trapped in lattice interstitials, and the second and third are in dislocations and vacancies.

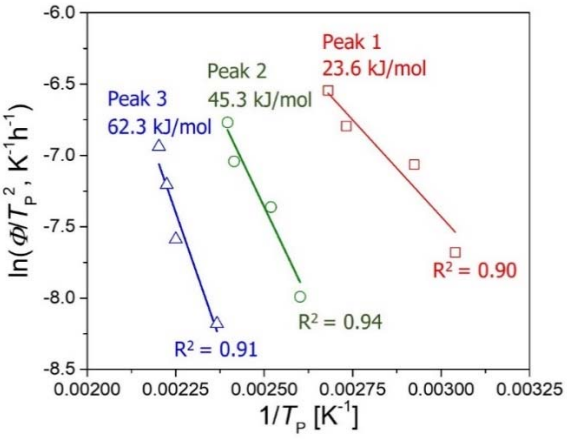


Fig. 12. Kissinger plots of deconvoluted peaks and the estimated activation energies for diffusible hydrogen desorption for as-built sample.

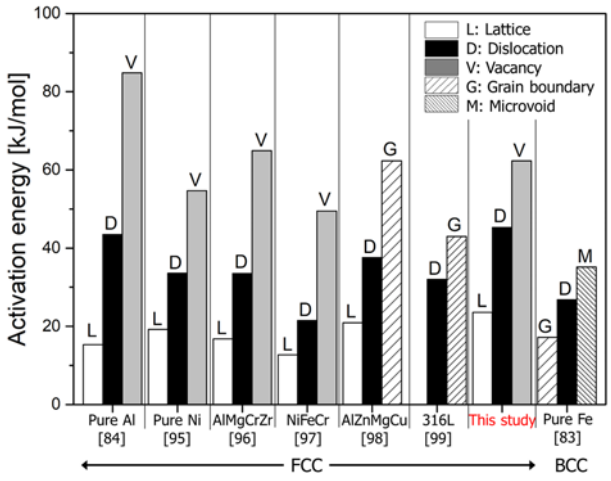


Fig. 13. Summary of activation energy values in the literatures.

For systematically analyzing the pre-straining effect, TDS experiments were also conducted on the sample taken from the gauge part of 15% (global) pre-strained specimen. Since it is impossible to prepare four TDS samples having exactly the same local strains

for four different heating rates, TDS test was performed only at 200 °C/h, as exhibited in Fig. 14. Interestingly, the hydrogen amount (21.15 wppm) in the pre-strained sample is similar to that in the as-built sample (18.23 wppm). While the accurate activation energy values for the pre-strained samples was not independently attainable, it is reasonable to assume that if three peaks can be deconvoluted from a low-temperature peak of 200 °C/h case in Fig. 14 and show similar temperature range to that in the as-built sample (Fig. 11), the peaks for pre-strained sample correspond to the same defects as those for the as-built sample; i.e., Peak 1, 2, and 3 for lattice, dislocation, and vacancy, respectively. This is simply because the activation energy associated with a specific crystalline defect is intrinsic and independent of the defect concentration.

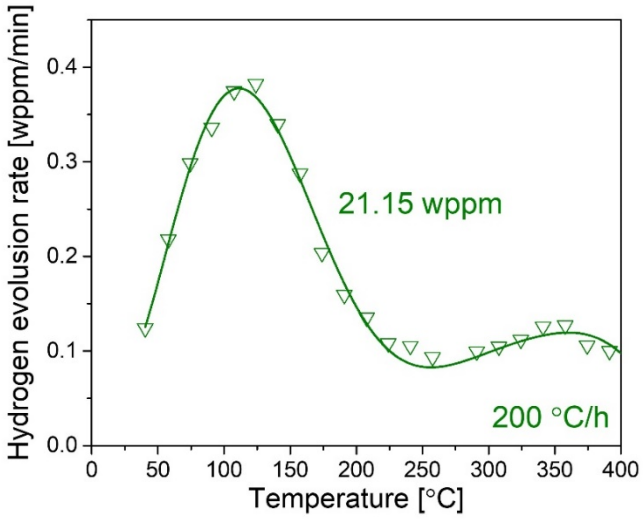


Fig. 14. TDS curve obtained from the pre-strained sample.

Fig. 15 compares the deconvolution peaks obtained from the as-built sample with those from the pre-strained sample. Three deconvoluted peaks for both samples were observed at similar temperature ranges as those in as-built samples, demonstrating that the three peaks also

correspond to lattice interstitial, dislocations, and vacancies, respectively. The most noteworthy feature in Fig. 15 is that, while three peaks appear in similar temperatures, the areas under them, which are proportional to the hydrogen amount, in the pre-strained sample is largely different from that in the as-built sample. The area fraction of each peak was calculated and also shown in Fig. 15. After pre-straining, the intensity of the "lattice" peak is reduced and that of the "dislocation" peak significantly increases, suggesting that the primary trapping sites for diffusible hydrogen may be transformed from distorted lattice to the dislocation in the pre-strained samples. Irrespective of this change, the impact of pre-straining on the total hydrogen content is not substantial, as the total amount of hydrogen (18.23 wppm for 200 °C/h, as shown in Fig. 9a) remains nearly constant even after pre-straining (21.15 wppm for 200 °C/h, as shown in Fig. 14). It is important to note that the "dislocations" in the figure is typical dislocations (including both statistically stored dislocations and geometrically necessary dislocations), not low-energy dislocations tangled in solidification cell walls [75][78]. As observed in Ag decorated as-built sample (Fig. 8), the cell walls may not be efficient trapping sites for diffusible hydrogen.

Based on these observations, we could conclude that the extent of change in mechanical properties due to hydrogen primarily depends on the total amount of diffusible hydrogen, regardless of which trap sites are dominant. In other words, the effect of diffusible hydrogen, whether trapped at interstitial lattice sites or dislocations, has a comparable impact on nanomechanical properties, at least in the present alloy.

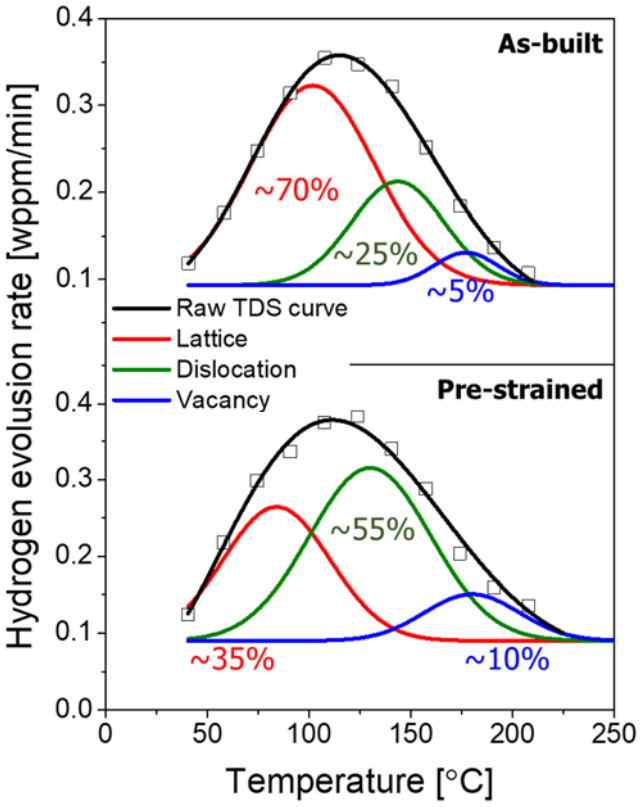


Fig. 15. Direct comparison of deconvoluted TDS curves in as-built and 15% (global) pre-strain samples.

## 6. Conclusion

In this study, we investigated the hydrogen trapping and its impact on the micromechanical properties of L-PBF fabricated CoCrFeNi HEA under as-built and pre-strained conditions, employing a nanoindentation and micro-tensile experiments combined with TDS analyses. Especially, we report for the first time, the diffusible H trapping behavior of AM HEA that is systematically investigated in a quantitative manner. The major findings are as follows.

- To analyze the influence of pre-straining with nanoindentation experiments, DIC-based local pre-strain measurement was adopted. It was found to be an effective way other than interrupted tensile tests for achieving different levels of global pre-stain.

- Nanoindentation results show that the influence of hydrogen on the mechanical properties of L-PBF HEA is insignificant. Somewhat surprisingly, pre-straining does not seem to affect this robust resistance to hydrogen-induced mechanical property variations.

- For understanding the absence of any influence of pre-straining on the hydrogenation effect, a detailed analysis of hydrogen trapping behavior was performed. From the deconvoluted TDS curves and estimated activation energy for hydrogen de-trapping, the trapping sites for diffusible hydrogen (which mainly affects the mechanical performance) were expected to be lattice, dislocations, and vacancies, while that for non-diffusible hydrogen might be micro-porosity that is inevitable in L-PBF processed samples.

- A change in the primary trapping site for diffusible hydrogen before and after pre-straining, transitioning from the distorted lattice structure in the as-built sample to the dislocations that prevail in pre-strained sample, was observed. Importantly, although pre-straining increases dislocation densities, the as-built and pre-strained samples exhibit a difference in primary hydrogen trapping sties but a similar quantity of hydrogen, leading to the conclusion that pre-straining does not exacerbate the already marginal hydrogen effect on the micromechanical properties in the as-built state.

**Acknowledgements**

The work at Hanyang University was supported by the National Research Foundation of Korea (NRF) grants funded by the Korea government (MSIT) (No. 2022R1A5A1030054 and RS-2023-00273384). The work at Chungnam National University was supported by the NRF grants funded by the MSIT (No. 2021R1F1A1048393). The work at IMRE (YZ) was supported by the Agency for Science, Technology and Research (A*STAR) of Singapore via Advanced Models for Additive Manufacturing (No. M22L2b0111). The work at Kagoshima University was supported by JSPS KAKENHI grant number 21K04694 (Grant-in-Aid for Scientific Research (C)). The work at POSTECH was supported by the NRF grant funded by the MSIP (No. 2021R1A2C3006662 and 2022R1A5A1030054). The work at NTU was supported by A*STAR via the Structural Metal Alloys Programme (No. A18B1b0061).

**References**


1. B. Cantor, I.T.H. Chang, P. Knight, A.J.B. Vincent, Microstructural development in equiatomic multicomponent alloys, Mater. Sci. Eng. A., 375 (2004) 213-218. https://doi.org/10.1016/j.msea.2003.10.257
2. J.W. Yeh, S.K. Chen, S.J. Lin, J.Y. Gan, T.S. Chin, T.T. Shun, C.H. Tsau, S.Y. Chang, Nanostructured high-entropy alloys with multiple principal elements: Novel alloy design concepts and outcomes, Adv. Eng. Mater., 6(5) (2004) 299-303. https://doi.org/10.1002/adem.200300567
3. D.B. Miracle, O.N. Senkov, A critical review of high entropy alloys and related concepts, Acta Mater., 122 (2017) 448-511. https://doi.org/10.1016/j.actamat.2016.08.081
4. Y. Zhang, T.T. Zuo, Z. Tang, M.C. Gao, K.A. Dahmen, P.K. Liaw, Z.P. Lu, Microstructures and properties of high-entropy alloys, Prog Mater Sci., 61 (2014) 1-93. https://doi.org/10.1016/j.pmatsci.2013.10.001
5. K.Y. Tsai, M.H. Tsai, J.W. Yeh, Sluggish diffusion in Co-Cr-Fe-Mn-Ni high-entropy alloys, Acta Mater., 61(13) (2013) 4887-4897. https://doi.org/10.1016/j.actamat.2013.04.058
6. Y. Brif, M. Thomas, I. Todd, The use of high-entropy alloys in additive manufacturing, Scr. Mater., 99 (2015) 93-96. https://doi.org/10.1016/j.scriptamat.2014.11.037
7. A. Piglione, B. Dovgyy, C. Liu, C.M. Gourlay, P.A. Hooper, M.S. Pham, Printability and microstructure of the CoCrFeMnNi high-entropy alloy fabricated by laser powder bed fusion, Mater. Lett., 224 (2018) 22-25. https://doi.org/10.1016/j.matlet.2018.04.052
8. A.O. Moghaddam, N.A. Shaburova, M.N. Samodurova, A. Abdollahzadeh, E.A. Trofimov, Additive manufacturing of high entropy alloys: A practical review, J. Mater. Sci. Technol., 77 (2021) 131-162. https://doi.org/10.1016/j.jmst.2020.11.029
9. W.E. Frazier, Metal Additive Manufacturing: A Review, J Mater. Eng. Perform., 23(6) (2014) 1917-1928. https://link.springer.com/article/10.1007/s11665-014-0958-z
10. W. Xu, M. Brandt, S. Sun, J. Elambasseril, Q. Liu, K. Latham, K. Xia, M. Qian, Additive manufacturing of strong and ductile Ti-6Al-4V by selective laser melting via in situ martensite decomposition, Acta Mater., 85 (2015) 74-84. https://doi.org/10.1016/j.actamat.2014.11.028
11. D. Herzog, V. Seyda, E. Wycisk, C. Emmelmann, Additive manufacturing of metals, Acta Mater., 117 (2016) 371-392. https://doi.org/10.1016/j.actamat.2016.07.019
12. M. Opprecht, J.P. Garandet, G. Roux, C. Flament, M. Soulier, A solution to the hot cracking problem for aluminium alloys manufactured by laser beam melting, Acta Mater., 197 (2020) 40-53. https://doi.org/10.1016/j.actamat.2020.07.015
13. S. Gorsse, C. Hutchinson, M. Gouné, R. Banerjee, Additive manufacturing of metals: a brief

review of the characteristic microstructures and properties of steels, Ti-6Al-4V and high-entropy alloys, Sci. Technol. Adv. Mat., 18 (1) (2017) 584-610.
https://doi.org/10.1080/14686996.2017.1361305

14. Z.H. Fu, B.J. Yang, K.F. Gan, D.S. Yan, Z.M. Li, G.Q. Gou, H. Chen, Z.R. Wang, Improving the hydrogen embrittlement resistance of a selective laser melted high-entropy alloy via modifying the cellular structures, Corros. Sci., 190 (2021) 109695.
https://doi.org/10.1016/j.corsci.2021.109695
15. Z. Xu, H. Zhang, X. Du, Y. He, H. Luo, G. Song, L. Mao, T. Zhou, L. Wang, Corrosion resistance enhancement of CoCrFeMnNi high-entropy alloy fabricated by additive manufacturing, Corros. Sci., 177 (2020) 108954.
https://doi.org/10.1016/j.corsci.2020.108954
16. Y.M. Wang, T. Voisin, J.T. McKeown, J.C. Ye, N.P. Calta, Z. Li, Z. Zeng, Y. Zhang, W. Chen, T.T. Roehling, R.T. Ott, M.K. Santala, P.J. Depond, M.J. Matthews, A.V. Hamza, T. Zhu, Additively manufactured hierarchical stainless steels with high strength and ductility, Nat. Mater., 17(1) (2018) 63-71.
https://doi.org/10.1038/nmat5021
17. T. Voisin, J.B. Forien, A. Perron, S. Aubry, N. Bertin, A. Samanta, A. Baker, Y.M. Wang, New insights on cellular structures strengthening mechanisms and thermal stability of an austenitic stainless steel fabricated by laser powder-bed-fusion, Acta Mater., 203 (2021) 116476.
https://doi.org/10.1016/j.actamat.2020.11.018
18. D.C. Kong, C.F. Dong, S.L. Wei, X.Q. Ni, L. Zhang, R.X. Li, L. Wang, C. Man, X.G. Li, About metastable cellular structure in additively manufactured austenitic stainless steels, Addit. Manuf., 38 (2021) 101804.
https://doi.org/10.1016/j.addma.2020.101804
19. S. Wei, Y. Zhao, B. Zhang, P. Wang, U. Ramamurty, Mesoscopic chemical heterogeneities in laser powder bed fused CoCrMo and Ni mixed powders and their effect on the mechanical properties. Mater. Sci. Eng. A, 888 (2023) 145795.
https://doi.org/10.1016/j.msea.2023.145795
20. Y.S. Chen, H.Z. Lu, J.T. Liang, A. Rosenthal, H.W. Liu, G. Sneddon, I. McCarroll, Z.Z. Zhao, W. Li, A.M. Guo, J.M. Cairney, Observation of hydrogen trapping at dislocations, grain boundaries, and precipitates, Science, 367 (2020) 171-177.
https://www.science.org/doi/full/10.1126/science.aaz0122
21. G. Jia, M. Lei, M. Li, W. Xu, R. Li, Y. Lu, M. Cai, Hydrogen embrittlement in hydrogen-blended natural gas transportation systems: a review, Int. J. Hydrog. Energy., 30 (2023) 32137-32157.
https://doi.org/10.1016/j.ijhydene.2023.04.266
22. H. Zhao, P. Chakraborty, D. Ponge, T. Hickel, B. Sun, C.H. Wu, B. Gault, D. Raabe, Hydrogen trapping and embrittlement in high-strength Al alloys, Nature, 602 (7897) (2022) 437-441.
https://doi.org/10.1038/s41586-021-04343-z
23. Y. Ding, H. Yu, M. Lin, K. Zhao, S. Xiao, A. Vinogradov, L. Qiao, M. Ortiz, J. He, Z. Zhang, Hydrogen-enhanced grain boundary vacancy stockpiling causes transgranular to intergranular fracture transition, Acta Mater., 239 (2022) 118279.

https://doi.org/10.1016/j.actamat.2022.118279
24. Y. Zhao, D.H. Lee, M.Y. Seok, J.A. Lee, M.P. Phaniraj, J.Y. Suh, H.Y. Ha, J.Y. Kim, U. Ramamurty, J.I. Jang, Resistance of CoCrFeMnNi high-entropy alloy to gaseous hydrogen embrittlement, Scr. Mater., 135 (2017) 54-58. https://doi.org/10.1016/j.scriptamat.2017.03.029
25. H. Luo, Z.M. Li, D. Raabe, Hydrogen enhances strength and ductility of an equiatomic high-entropy alloy, Sci. Rep., 7 (2017) 9892. https://doi.org/10.1038/s41598-017-10774-4
26. Y. Zhao, D.H. Lee, W.J. Kim, M.Y. Seok, J.Y. Kim, H.N. Han, J.Y. Suh, U. Ramamurty, J.I. Jang, Influence of pre-strain on the gaseous hydrogen embrittlement resistance of a high-entropy alloy, Mater. Sci. Eng. A, 718 (2018) 43-47. https://doi.org/10.1016/j.msea.2018.01.107
27. Z. Xu, H. Zhang, X. Du, Y. He, H. Luo, G. Song, L. Mao, T. Zhou, L. Wang, Corrosion resistance enhancement of CoCrFeMnNi high-entropy alloy fabricated by additive manufacturing, Corros. Sci., 177 (2020) 108954. https://doi.org/10.1016/j.corsci.2020.108954
28. Y.-.T. Lin, X. An, Z. Zhu, M.L.S. Nai, C.-.W. Tsai, H.-.W. Yen, Effect of cell wall on hydrogen response in CoCrFeMnNi high-entropy alloy additively manufactured by selective laser melting, J. Alloys Compd., 925 (2022) 166735. https://doi.org/10.1016/j.jallcom.2022.166735
29. D. Wan, S. Guan, D. Wang, X. Lu, J. Ma, Hydrogen embrittlement of additively manufactured AlCoCrFeNi2.1 eutectic high-entropy alloy, Corros. Sci., 195 (2022) 110007. https://doi.org/10.1016/j.corsci.2021.110007
30. D.H. Lee, J.Y. Jung, K.H. Lee, S.Y. Lee, Y. Zhao, K.B. Lau, P. Wang, U. Ramamurty, Distinct effects of in-situ and ex-situ hydrogen charging methods on the mechanical behavior of CoCrFeNi high-entropy alloy fabricated by laser-powder bed fusion, J. Alloy. Compd., 940 (2023) 168858. https://doi.org/10.1016/j.jallcom.2023.168858
31. S.H. Li, Y. Zhao, J. Radhakrishnan, U. Ramamurty, A micropillar compression investigation into the plastic flow properties of additively manufactured alloys, Acta Mater., 240 (2022) 118290. https://doi.org/10.1016/j.actamat.2022.118290
32. S.H. Li, Y. Zhao, U. Ramamurty, Role of the solidification cells on the yield strength of the Al-Si-Mg alloy manufactured using laser powder bed fusion: a micropillar compression study, Scr. Mater., 234 (2023) 115566. https://doi.org/10.1016/j.scriptamat.2023.115566
33. J. Crank, The Mathematics of Diffusion, second ed., Oxford University Press, London, 1979.
34. A.E. Pontini, J.D. Hermida, A.E. Pontini, J.D. Hermida, X-ray diffraction measurement of the stacking fault energy reduction induced by hydrogen in an AISI 304 steel, Scr. Mater. 37 (1997) 1831-1837. https://doi.org/10.1016/S1359-6462(97)00332-1
35. Y. Zhao, J.M. Park, D.H. Lee, E.J. Song, J.Y. Suh, U. Ramamurty, J. il Jang, Influences of hydrogen charging method on the hydrogen distribution and nanomechanical properties of

face-centered cubic high-entropy alloy: a comparative study, Scr. Mater., 168 (2019) 76-80. https://doi.org/10.1016/j.scriptamat.2019.04.025
36. Tsong-Pyng Perng, C.J. Altstetter, Effects of deformation on hydrogen permeation in austenitic stainless steels, Acta Metallurgica, 34 (1986) 1771-1781. https://doi.org/10.1016/0001-6160(86)90123-9
37. C. San Marchi, B.P. Somerday, S.L. Robinson, Permeability, solubility and diffusivity of hydrogen isotopes in stainless steels at high gas pressures, Int. J. Hydrog. Energy., 32 (2007) 100-116 https://doi.org/10.1016/j.ijhydene.2006.05.008
38. Junichiro Yamabe, Osamu Takakuwa, Hisao Matsunaga, Hisatake Itoga, Saburo Matsuoka, Hydrogen diffusivity and tensile-ductility loss of solution-treated austenitic stainless steels with external and internal hydrogen, Int. J. Hydrog. Energy., 42 (2017) 13289-13299. https://doi.org/10.1016/j.ijhydene.2017.04.055
39. K.E. Nygren, K.M. Bertsch, S. Wang, H. Bei, A. Nagao, I.M. Robertson, Hydrogen embrittlement in compositionally complex FeNiCoCrMn FCC solid solution alloy, Curr. Opin. Solid State Mater. Sci., 22 (2018) 1-7. https://doi.org/10.1016/j.cossms.2017.11.002
40. M. Koyama, H.Y. Wang, V.K. Verma, K. Tsuzaki, E. Akiyama, Effects of Mn Content and Grain Size on Hydrogen Embrittlement Susceptibility of Face-Centered Cubic High-Entropy Alloys, Metall. Mater. Trans, A, 51(11) (2020) 5612-5616. https://doi.org/10.1007/s11661-020-05966-z
41. Y. Zhao, J.-M. Park, K. Murakami, S. Komazaki, M. Kawasaki, K. Tsuchiya, J.-Y. Suh, U. Ramamurty, J. Jang, Exploring the hydrogen absorption and strengthening behavior in nanocrystalline face-centered cubic high-entropy alloys, Scr. Mater., 203 (2021) 114069. https://doi.org/10.1016/j.scriptamat.2021.114069
42. Y. Mine, C. Narazaki, K. Murakami, S. Matsuoka, Y. Murakami, Hydrogen transport in solution-treated and pre-strained austenitic stainless steels and its role in hydrogen-enhanced fatigue crack growth, Int. J. Hydrog. Energy., 34 (2009) 1097-1107. https://doi.org/10.1016/j.ijhydene.2008.11.018
43. Thorsten Michler, Joerg Naumann, Martin Hock, Karl Berreth, Michael P. Balogh, Erich Sattler, Microstructural properties controlling hydrogen environment embrittlement of cold worked 316 type austenitic stainless steels, Mater. Sci. Eng. A., 628 (2015) 252-261. https://doi.org/10.1016/j.msea.2015.01.054
44. Chengshuang Zhou, Yangyang Song, Qiaoying Shi, Shiyin Hu, Jinyang Zheng, Peng Xu, Lin Zhang, Effect of pre-strain on hydrogen embrittlement of metastable austenitic stainless steel under different hydrogen conditions, Int. J. Hydrog. Energy., 44 (2019) 26036-26048 https://doi.org/10.1016/j.ijhydene.2019.08.046
45. H. Ji, I.-J. Park, S.-.M. Lee, Y.-.K. Lee, The effect of pre-strain on hydrogen embrittlement in 310S stainless steel, J. Alloys Compd., 598 (2014) 205-212. https://doi.org/10.1016/j.jallcom.2014.02.038
46. X. Li, Y. Wang, P. Zhang, B. Li, X. Song, J. Chen, Effect of pre-strain on hydrogen embrittlement of high strength steels, Mater. Sci. Eng. A, 616 (2014) 116-122. https://doi.org/10.1016/j.msea.2014.07.085

47. S.H. Yu, S.M. Lee, S. Lee, J.H. Nam, J.S. Lee, C.M. Bae, Effects of lamellar structure on tensile properties and resistance to hydrogen embrittlement of pearlitic steel, Acta Mater., 172 (2019) 92-101.
https://doi.org/10.1016/j.actamat.2019.04.040
48. Y. Wang, X. Wang, J. Gong, L. Shen, W. Dong, Hydrogen embrittlement of catholically hydrogen-precharged 304L austenitic stainless steel: effect of plastic pre-strain, Int. J. Hydrog. Energy, 39 (25) (2014) 13909-13918.
https://doi.org/10.1016/j.ijhydene.2014.04.122
49. X.Z. Liang, M.F. Dodge, S. Kabra, J.F. Kelleher, T.L. Lee, H.B. Dong, Effect of hydrogen charging on dislocation multiplication in pre-strained super duplex stainless steel, Scr. Mater., 143 (2018) 20-24.
https://doi.org/10.1016/j.scriptamat.2017.09.001
50. Y. Zhao, J.-M. Park, J.i. Jang, U. Ramamurty, Bimodality of incipient plastic strength in face-centered cubic high-entropy alloys, Acta Mater., 202 (2021) 124-134.
https://doi.org/10.1016/j.actamat.2020.10.066
51. Guoqing Huang, Bo Li, Yinan Chen, Fuzhen Xuan, Nanotwining induced by tensile fatigue and dynamic impact of laser powder bed fusion additively manufactured CoCrFeNi high-entropy alloy, J. Mater. Sci. Technol., 183 (2024) 241-257.
https://doi.org/10.1016/j.jmst.2023.10.028
52. Yinan Chen, Bo Li, Bo Chen, Fuzhen Xuan, High-cycle fatigue induced twinning in CoCrFeNi high-entropy alloy processed by laser powder bed fusion additive manufacturing, Addit. Manuf., 61 (2023) 103319.
https://doi.org/10.1016/j.addma.2022.103319
53. Yingbo Peng, Caijun Jia, Lingfeng Song, Yuchao Bian, Hongwei Tang, Guanglu Cai, Gaoyan Zhong, The manufacturing process optimization and the mechanical properties of FeCoCrNi high entropy alloys fabricated by selective laser melting, Intermetallics, 145 (2022) 107557.
https://doi.org/10.1016/j.intermet.2022.107557
54. Danyang Lin, Lianyong Xu, Hongyang Jing, Yongdian Han, Lei Zhao, Yankun Zhang, Huan Li, A strong, ductile, high-entropy FeCoCrNi alloy with fine grains fabricated via additive manufacturing and a single cold deformation and annealing cycle, Addit. Manuf., 36 (2020) 101591.
https://doi.org/10.1016/j.addma.2020.101591
55. Yongyun Zhang, Congrui Yang, Haibo Ke, K.C. Chan, Weihua Wang, A study on the microstructure and mechanical behavior of CoCrFeNi high entropy alloy fabricated via laser powder bed fusion: Experiment and crystal plasticity finite element modelling, Mater. Sci. Eng. A., 893 (2024) 146111.
https://doi.org/10.1016/j.msea.2024.146111
56. Z.H. Xiong, S.L. Liu, S.F. Li, Y. Shi, Y.F. Yang, R.D.K. Misra, Role of melt pool boundary condition in determining the mechanical properties of selective laser melting AlSi10Mg alloy, Mater. Sci. Eng. A, 740 (2019) 148-156.
https://doi.org/10.1016/j.msea.2018.10.083
57. G.M. Karthik, H.S. Kim, Heterogeneous Aspects of Additive Manufactured Metallic Parts: A

Review, Met. Mater. Int., 27(1) (2021) 1-39.
https://doi.org/10.1007/s12540-020-00931-2
58. Shang Sui, Jing Chen, Rui Zhang, Xianliang Ming, Fencheng Liu, Xin Lin, The tensile deformation behavior of laser repaired Inconel 718 with a non-uniform microstructure, Mater. Sci. Eng. A., 688 (2017) 480-487.
https://doi.org/10.1016/j.msea.2017.01.110
59. Yangchuan Cai, Yan Cui, Sunusi Marwana Manladan, Lisong Zhu, Mengdie Shan, Da Sun, Jian Han, Mechanism for the Improvement of the Mechanical Properties of FeCoCrNi+FeCoCrNiAl-Laminated HEA Fabricated by Laser Melting Deposition, JOM, 74 (2022) 2860-2870.
https://doi.org/10.1007/s11837-022-05263-7
60. Joakim Karlsson, Torsten Sjögren, Anders Snis, Håkan Engqvist, Jukka Lausmaa, Digital image correlation analysis of local strain fields on Ti6Al4V manufactured by electron beam melting, Mater. Sci. Eng. A., 618 (2014) 456-461.
https://doi.org/10.1016/j.msea.2014.09.022
61. G.K. Williamson, W.H. Hall, X-ray line broadening from filed aluminium and wolfram, Acta Metall., 1 (1953) 22-31.
https://doi.org/10.1016/0001-6160(53)90006-6
62. T. Ungar, A. Revesz, A. Borbely, Dislocations and grain size in electrodeposited nanocrystalline Ni determined by the modified Williamson-Hall and Warren-Averbach procedures, J Appl. Crystallogr., 31 (1998) 554-558.
https://doi.org/10.1107/S0021889897019559
63. Z. Gao, Y. Zhao, J.M. Park, A.H. Jeon, K. Murakami, S.I. Komazaki, K. Tsuchiya, U. Ramamurty, J.I. Jang, Decoupling the roles of constituent phases in the strengthening of hydrogenated nanocrystalline dual-phase high-entropy alloys, Scr. Mater., 210 (2022) 114472.
https://doi.org/10.1016/j.scriptamat.2021.114472
64. Y.K. Kim, J. Cho, K.A. Lee, Selective laser melted equiatomic CoCrFeMnNi high-entropy alloy: Microstructure, anisotropic mechanical response, and multiple strengthening mechanism, J. Alloys Compd., 805 (2019) 680-691.
https://doi.org/10.1016/j.jallcom.2019.07.106
65. S.-H. Li, Y. Zhao, J. Radhakrishnan, U. Ramamurty, A micropillar compression investigation into the plastic flow properties of additively manufactured alloys, Acta Mater. 240 (2022) 118290.
https://doi.org/10.1016/j.actamat.2022.118290
66. S. Zaefferer, N.-N. Elhami, Theory and application of electron channelling contrast imaging under controlled diffraction conditions, Acta Mater, 75 (2014) 20-50.
https://doi.org/10.1016/j.actamat.2014.04.018
67. J. Jang, G.M. Pharr, Influence of indenter angle on cracking in Si and Ge during nanoindentation, Acta Mater., 56(16) (2008) 4458-4469.
https://doi.org/10.1016/j.actamat.2008.05.005
68. Y. Zhao, I.C. Choi, M.Y. Seok, M.H. Kim, D.H. Kim, U. Ramamurty, J.Y. Suh, J.I. Jang, Effect of hydrogen on the yielding behavior and shear transformation zone volume in metallic glass ribbons, Acta Mater., 78 (2014) 213-221.

https://doi.org/10.1016/j.actamat.2014.06.046
69. A. Bolshakov, G.M. Pharr, Influences of pileup on the measurement of mechanical properties by load and depth sensing indentation techniques, J Mater. Res., 13 (4) (1998) 1049-1058. https://doi.org/10.1557/JMR.1998.0146
70. A. Barnoush, Correlation between dislocation density and nanomechanical response during nanoindentation, Acta Mater., 60(3) (2012) 1268-1277. https://doi.org/10.1016/j.actamat.2011.11.034
71. Jannik C. Meyer, C. O. Girit, M. F. Crommie, A. Zettl, Imaging and dynamics of light atoms and molecules on graphene, Nature, 454 (2008) 319-322. https://doi.org/10.1038/nature07094
72. Y.S. Chen, D. Haley, S.S. Gerstl, A.J. London, F. Sweeney, R.A. Wepf, W.M. Rainforth, P.A. Bagot, M.P. Moody Direct observation of individual hydrogen atoms at trapping sites in a ferritic steel Science, 355 (6330) (2017) 1196-1199. https://doi.org/10.1016/j.actamat.2020.09.031
73. Z. Tarzimoghadam, M. Rohwerder, S.V. Merzlikin, A. Bashir, L. Yedra, S. Eswara, D. Ponge, D. Raabe, Multi-scale and spatially resolved hydrogen mapping in a Ni-Nb model alloy reveals the role of the 8 phase in hydrogen embrittlement of alloy 718, Acta Mater., 109 (2016) 69-81. https://doi.org/10.1016/j.actamat.2016.02.053
74. J. Ovejerogarcia, Hydrogen Microprint Technique in the Study of Hydrogen in Steels, J. Mater. Sci., 20(7) (1985) 2623-2629. https://doi.org/10.1007/BF00556094
75. D.-H. Lee, Y. Zhao, S.Y. Lee, D. Ponge, E.A. Jägle, Hydrogen-assisted failure in Inconel 718 fabricated by laser powder b e d fusion: The role of solidification substructure in the embrittlement, Scr. Mater. 207 (2022) 114308. https://doi.org/10.1016/j.scriptamat.2021.114308
76. H. Ji, I.-J. Park, S.-M. Lee, Y.-K. Lee, The effect of pre-strain on hydrogen embrittlement in 310S stainless Steel, J. Alloys. Compd., 598 (2014) 205. https://doi.org/10.1016/j.jallcom.2014.02.038
77. D.-H. Lee, B. Sun, S. Lee, D. Ponge, E.A. Jägle, D. Raabe, Comparative study of hydrogen embrittlement resistance between additively and conventionally manufactured 304L austenitic stainless steels, Mater. Sci. Eng. A, 803 (2021)140499. https://doi.org/10.1016/j.msea.2020.140499
78. J.-M. Park, Y. Zhao, T. Voisin, D.-H. Lee, S.-i Komazaki, Y. Ko, D.-I. Kim, J.-Y. Suh, H.N. Han, Y.M. Wang, U. Ramamurty, J.-i Jang, Hydrogen uptake and its influence in selective laser melted austenitic stainless steel: A nanoindentation study, Scr. Mater., 194 (2021) 113718. https://doi.org/10.1016/j.scriptamat.2020.113718
79. S.W. Baek, E.J. Song, J.H. Kim, M. Jung, U.B. Baek, S.H. Nahm, Hydrogen embrittlement of 3-D printing manufactured austenitic stainless steel part for hydrogen service, Scr. Mater., 130 (2017) 87-90. https://doi.org/10.1016/j.scriptamat.2016.11.020
80. I. Maroef, D.L. Olson, M. Eberhart, G.R. Edwards, Hydrogen trapping in ferritic steel weld metal, Int. Mater. Rev., 47 (2002) 191-223.

https://doi.org/10.1179/095066002225006548
81. S.K. Lawrence, Y. Yagodzinskyy, H. Hänninen, E. Korhonen, E. Tuomisto, Z. Harris, B.P. Somerday, Effects of grain size and deformation temperature on hydrogen-enhanced vacancy formation in Ni alloys, Acta Mater., 128 (2017) 218-226. https://doi.org/10.1016/j.actamat.2017.02.016
82. X. Zhu, W. Li, T. Hsu, S. Zhou, L. Wang, X. Jin, Improved resistance to hydrogen embrittlement in a high-strength steel by quenching–partitioning–tempering treatment, Scr. Mater., 97 (2015) 21-24. https://doi.org/10.1016/j.scriptamat.2014.10.030
83. W.Y. Choo, J.Y. Lee, Thermal-Analysis of Trapped Hydrogen in Pure Iron, Metall. Trans. A, 13(1) (1982) 135-140. https://doi.org/10.1007/BF02642424
84. G.A. Young, J.R. Scully, The diffusion and trapping of hydrogen in high purity aluminum, Acta Mater., 46(18) (1998) 6337-6349. https://doi.org/10.1016/S1359-6454(98)00333-4
85. H.K. Dharamshi, H. Bhadeshia, Prevention of hydrogen embrittlement in steels, ISIJ Int., 56 (1) (2016) 24-36. https://doi.org/10.2355/isijinternational.ISIJINT-2015-430
86. D. Rudomilova, T. Prosek, G. Luckeneder, Techniques for investigation of hydrogen embrittlement of advanced high strength steels, Corros. Rev., 36 (2018) 413-434. https://doi.org/10.1515/corrrev-2017-0106
87. S.K. Dwivedi, M. Vishwakarma, Effect of hydrogen in advanced high strength steel materials, Int. J. Hydrog. Energy, 44 (2019) 28007-28030. https://doi.org/10.1016/j.ijhydene.2019.08.149
88. X. Li, J. Yin, J. Zhang, Y. Wang, X. Song, Y. Zhang, Hydrogen embrittlement and failure mechanisms of multi-principal element alloys: a review, J. Mater. Sci. Technol., 122 (2022) 20-32. https://doi.org/10.1016/j.jmst.2022.01.008
89. S. Zhang, E. Fan, J. Wan, J. Liu, Y. Huang, X. Li, Effect of Nb on the hydrogen-induced cracking of high-strength low-alloy steel, Corros. Sci., 139 (2018) 83-96. https://doi.org/10.1016/j.corsci.2018.04.041
90. R.A. Oriani, P.H. Josephic, Equilibrium Aspects of Hydrogen-Induced Cracking of Steels, Acta Metall. Mater., 22(9) (1974) 1065-1074. https://doi.org/10.1016/0001-6160(74)90061-3
91. S.P. Lynch, Environmentally Assisted Cracking - Overview of Evidence for an Adsorption-Induced Localized-Slip Process, Acta Metall Mater., 36(10) (1988) 2639-2661. https://doi.org/10.1016/0001-6160(88)90113-7
92. H. Shoda, H. Suzuki, K. Takai, Y. Hagihara, Hydrogen Desorption Behavior of Pure Iron and Inconel 625 during Elastic and Plastic Deformation, ISIJ Int., 50 (1) (2010) 115-123. https://doi.org/10.2355/isijinternational.50.115
93. P. Metalnikov, D. Eliezer, G. Ben-Hamu, Hydrogen trapping in additive manufactured Ti-6Al-4V alloy, Mater. Sci. Eng. A, 811 (2021) 141050. https://doi.org/10.1016/j.msea.2021.141050

94. J.Y. Lee, S.M. Lee, Hydrogen Trapping Phenomena in Metals with Bcc and Fcc Crystal-Structures by the Desorption Thermal-Analysis Technique, Surf. Coat. Technol., 28(3-4) (1986) 301-314.
https://doi.org/10.1016/0257-8972(86)90087-3
95. A. Oudriss, J. Creus, J. Bouhattate, E. Conforto, C. Berziou, C. Savall, X. Feaugas, Grain size and grain-boundary effects on diffusion and trapping of hydrogen in pure nickel, Acta Mater., 60(19) (2012) 6814-6828.
https://doi.org/10.1016/j.actamat.2012.09.004
96. M. Safyari, M. Moshtaghi, T. Hojo, E. Akiyama, Mechanisms of hydrogen embrittlement in high-strength aluminum alloys containing coherent or incoherent dispersoids, Corros. Sci., 194 (2022) 109895.
https://doi.org/10.1016/j.corsci.2021.109895
97. M. Moshtaghi, M. Safyari, G. Mori, Combined thermal desorption spectroscopy, hydrogen visualization, HRTEM and EBSD investigation of a Ni-Fe-Cr alloy: The role of hydrogen trapping behavior in hydrogen-assisted fracture, Mater. Sci. Eng. A, 848 (2022) 143428.
https://doi.org/10.1016/j.jmrt.2022.11.111
98. M. Moshtaghi, M. Safyari, S. Kuramoto, T. Hojo, Unraveling the effect of dislocations and deformation-induced boundaries on environmental hydrogen embrittlement behavior of a cold-rolled Al-Zn-Mg-Cu alloy, Int. J. Hydrog. Energy, 46(11) (2021) 8285-8299.
https://doi.org/10.1016/j.ijhydene.2020.12.028
99. R. Silverstein, D. Eliezer, Mechanisms of hydrogen trapping in austenitic, duplex, and super martensitic stainless steels, J. Alloys Compd., 720 (2017) 451-459.
https://doi.org/10.1016/j.jallcom.2017.05.286
100. K.H. So, J.S. Kim, Y.S. Chun, K.-T. Park, Y.-K. Lee, C.S. Lee, Hydrogen delayed fracture properties and internal hydrogen behavior of a Fe-18Mn-1.5 Al-0.6 C TWIP steel, ISIJ Int., 49 (2009) 1952-1959.
https://doi.org/10.2355/isijinternational.49.1952
101. B. Sun, W. Krieger, M. Rohwerder, D. Ponge, D. Raabe, Dependence of hydrogen embrittlement mechanisms on microstructure-driven hydrogen distribution in medium Mn steels, Acta Mater., 183 (2020) 313-328.
https://doi.org/10.1016/j.actamat.2019.11.029